Sigma Journal of Engineering and Natural Sciences
Web page info: https://sigma.yildiz.edu.tr
DOI: 10.14744/sigma.2024.00009

Research Article

LYS semi-supported plate as a ductile end-diaphragm in steel girder bridges

Morteza JAMSHIDI[1,*]

[1]*Faculty of Engineering, Islamic Azad University, Chalous, 46615397, Iran*

ARTICLE INFO

Article history
Received: 09 January 2022
Revised: 05 February 2022
Accepted: 21 June 2022

Keywords:
Steel Bridge; Steel Plate; End Diaphragm; Seismic Design; Low-Yield Steel

ABSTRACT

Ductile end diaphragms have been suggested as an appropriate device in the past to improve the seismic response of steel girder bridges. This paper investigates the efficiency of the seismic design strategy that utilized a slab-connected steel plate as a ductile diaphragm in the superstructure. Protecting the main girder from typically reported damage and mitigating the transferred lateral load to the non-ductile substructures are the main objectives of this study. The results show that a slab-connected thin steel plate with low yielding stress (LYS) can mitigate the force demand on the non-ductile substructures and act as a structural fuse. It can also reduce the transverse displacement of the superstructure and, consequently, prevent the end of the main girder from buckling and/or yielding.

Cite this article as: Jamshidi M. LYS semi-supported plate as a ductile end-diaphragm in steel girder bridges. Sigma J Eng Nat Sci 2024;42(1):70–81.

INTRODUCTION

Past study has shown the vulnerability of steel girder bridges [1-3]. Hence, some studies were conducted to determine the lateral load path and define a critical component of the superstructure. Preliminary analyses revealed the effect of the end diaphragm and also the effect of bearing stiffeners on the maximum lateral displacement of steel girder bridges [4, 5]. In 1996, the application of ductile end diaphragms in steel bridge superstructures was suggested [6]. It was found that only the end diaphragm and a part of the steel girder including the bearing stiffeners (adjacent to the supports), were the main segment of the lateral load resistance system of the steel girder bridges [7, 8]. Furthermore, due to the reason that more practical ductile diaphragm sizes are designed when only one energy-dissipation device is located at each end, only two steel girders are connected by a ductile end diaphragm are needed to be studied [9]. In 1999, triangular-plate added damping and stiffness (TADAS) shear panel system (SPS) and eccentrically braced frames (EBF) were used as ductile end diaphragms [10]. Carden et al. [11, 12] applied buckling-restrained braces (BRB) and single-angle X braces as a ductile end diaphragm. Jamshidi et al. [5, 8] proposed the use of steel plates as a ductile diaphragm in steel girder bridges. In 2019 the effect of this strategy was also approved in steel tube girder bridges [13]. In Jamshidi studies, the vertical edges of the infill plate were connected to the bearing stiffeners (which are primary elements of the gravity load caring system). Thin infill plate end diaphragms

*Corresponding author.
*E-mail address: m.jamshidi@iauc.ac.ir , jamshidi.iauc@gmail.com

This paper was recommended for publication in revised form by Regional Editor Ahmet Selim Dalkilic

buckled in shear at low lateral displacement and the extension of the tension field caused severe stress on the bearing stiffeners as vertical boundary elements. This may lead to the main girder damage and consequently, bridges collapse. In the building structures to mitigate vertical boundary demands, steel plates are only connected to the beam [14-17]. By patterning this idea, the infill plate is only connected to the concrete slabs to improve the seismic response of the thin steel infill end diaphragm.

However, there is no adequate guidance to calculate the ductility, force reduction factor, and stiffness of the semi-supported steel plate end diaphragms for steel bridges. Hence, this study is conducted to determine the efficiency of semi-supported LYS plate end diaphragm as a retrofit methodology using force reduction factor and also investigate the effect of LYS plate end diaphragm as a structural fuse using ductility coefficient.

METHOD OF STUDY

Models

In this study, the span of a 40-m steel girder bridge with a width of 8 m was considered. The full composite action between a reinforced concrete slab with 200-mm-thickness and steel girders (WWF 1200×333) spaced at 2 m was assumed. This bridge does not have the benefit of underside bracing. The bridge was designed by Dicleli and Bruneau [18] with respect to the strength requirements of the 1961 edition of the American Association of State Highway Officials [19]. Based on the experimental and numerical studies, the main part of the seismic load is transferred to the substructure through the end of the span [4, 20, 21]. Therefore, analysing the end diaphragm panel can appropriately represent the seismic behaviour of the bridge. Hence the stub of the steel girder bridge, consisting of the end diaphragm, the bearing stiffener, and a part of the steel girder (500 mm) (Figure 1) were used to study the use of semi-supported steel plates in steel girder bridges as an energy dissipation device by varying the infill plate thickness (t_w = 3, 5, and 7 mm), length (l_w=540, 1080 and 1744 mm) and material properties of the steel plate (S1, S2) (Table 1). Horizontal boundary elements (HBEs) (W150×37) and bottom and top chords (2L55×55×5) were designed based on the requirements of the AISC Design Guide 20 [22] to permit the extension of yield lines across the semi-supported steel plate, to resist the corresponding tension from the plate, and to stay in the elastic range. The bottom and top chords were fastened to the adjoining concrete components via adequate bolts. Two 20× 30× 2 mm box sections of 735.6 mm height located at a distance of 20 mm from the horizontal boundary elements were used for stiffening the free edges and preventing more out of plane deformations of thin infill plates due to shear buckling.

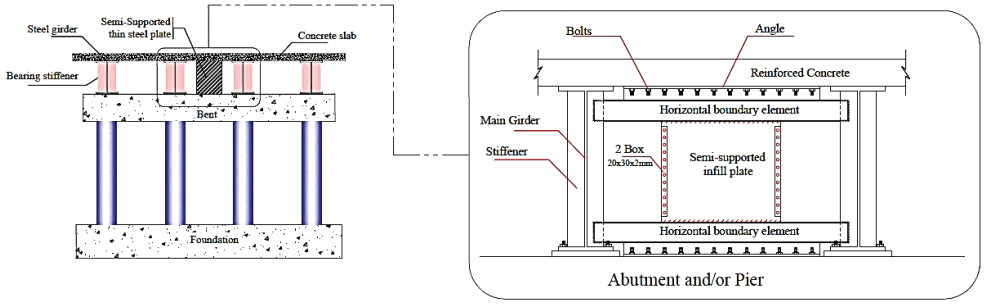

Figure 1. Semi-supported steel infill plate as a ductile end diaphragm.

Table 1. Definition of studied models

Name of Models	Lw (mm)	tw (mm)	Name of Material	Name of Models	Lw (mm)	tw (mm)	Name of Material
0540-t3-Fy86	540	3	S1	0540-t5-Fy165	540	5	S2
1080-t3-Fy86	1080	3	S1	1080-t5-Fy165	1080	5	S2
1744-t3-Fy86	1744	3	S1	1744-t5-Fy165	1744	5	S2
0540-t3-Fy165	540	3	S2	0540-t7-Fy86	540	7	S1
1080-t3-Fy165	1080	3	S2	1080-t7-Fy86	1080	7	S1
1744-t3-Fy165	1744	3	S2	1744-t7-Fy86	1744	7	S1
0540-t5-Fy86	540	5	S1	0540-t7-Fy165	540	7	S2
1080-t5-Fy86	1080	5	S1	1080-t7-Fy165	1080	7	S2
1744-t5-Fy86	1744	5	S1	1744-t7-Fy165	1744	7	S2

Material Property

The stress-strain curve, which is adapted from the experimental research of Zahrai and Bruneau [23], was used to investigate the effects of the nonlinear material properties of bearing stiffeners, HBEs, and steel girders on the finite element (FE) studies (Figure 2 (a)). Moreover, semi-supported LYS infill plates with various material properties were applied as end diaphragms (Table 2). The infill plate materials are elastic-plastic models with a linear strain hardening ratio (H/E) (Figure 2 (b)). For all steel materials, the Poisson's ratio and module of elasticity equal 0.3 and 200 GPa, respectively. In this research, all the materials follow the combined hardening rule, and the Von-Mises yield criterion is used to show the yielding of the metal materials.

Numerical Modelling

Buckling and incremental nonlinear pushover analyses were conducted using ABAQUS FE software. The bearing stiffeners, steel girders, infill plates, and horizontal boundary elements were modelled and meshed using 4-node doubly curved thin shell (S4R) with reduced integration, hourglass control and finite membrane strains. An 8-node linear brick (C3D8R) with reduced integration and hourglass control was used to mesh the concrete slab (Figure 3).

Quad element shape with standard technique was used to mesh control of diaphragm elements and the finite element size ranging from 35 to 50 mm. Minimize the mesh transition option is also used during the meshing process. In certain cases, this option will help to reduce the mesh distortion. However, the mesh may deviate farther from the specified seeds.

To study the effect of meshing size in the analysis process, the capacity curve of the model 1080-t5-Fy86

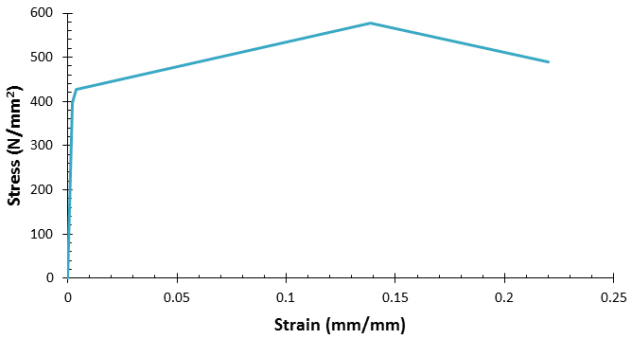

(a) Stress-strain diagram for boundary elements

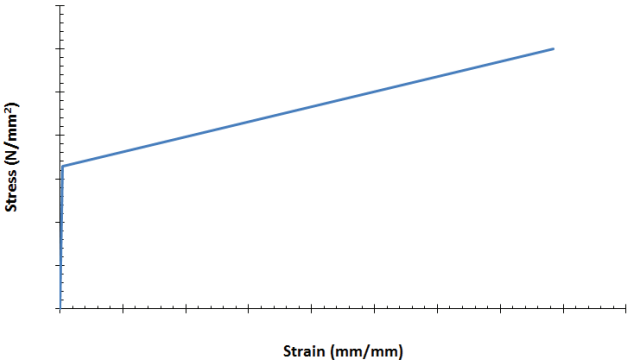

(b) Typical stress-strain diagram for in-fill plates

Figure 2. Material properties.

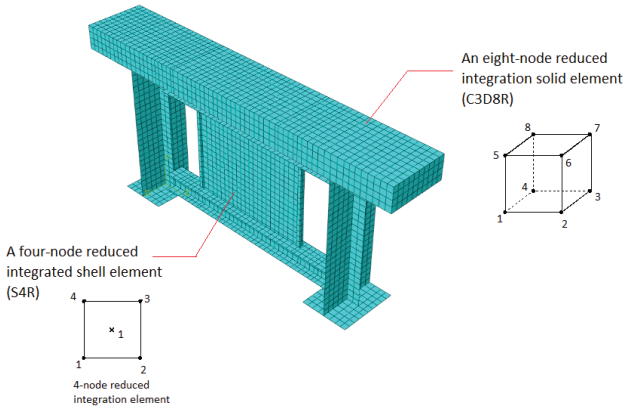

Figure 3. Element type in the numerical analysis.

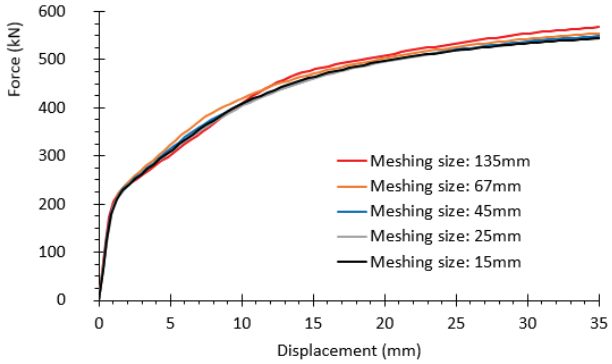

Figure 4. The capacity curve of the model 1080-t5-Fy86 with different meshing size.

Table 2. Various types of LYS material applied as infill plates

Name of material	Initial yield stress (N/mm²)	Ultimate strength (N/mm²)	Strain-hardening ratio
S1	86	254	0.00433
S2	165	300	0.00433

was extracted in five different cases (in terms of the meshing size). As the meshing size increases, the difference between the capacity curves (for the displacement of more than 10 mm) will increase; as far as the force corresponding to the 35 mm displacement of the model with a meshing size of 150 mm is equal to 567 kN which is about 4% more than the corresponding force of the models with the mesh dimensions of less than 50 mm (Figure 4). Therefore, the meshing size is limited to less than 50 mm in this paper.

A reduced integration formulation was applied to obtain more precise results and to decrease computing time. Furthermore, the inclusion of nonlinear effects of large displacements was considered. The shear connector was modelled using zero-length spring elements throughout the steel girder to define the composite action among the steel girders and the concrete slab. As shown in Figure 5, there are four supporting points each main girder. For all these supporting points, the displacement in all directions and also rotation around all axes (except Y axes) were restricted. A lateral load was applied to the FE specimen through the displacement of the concrete slab, which was gradually enhanced from zero to a target displacement that corresponded to 3% of the steel girder height (Figure 5). This was conducted through the static-general analysis with a time period of 100 and 0.1 maximum increment size.

Validation of Numerical Modelling

To the authors' knowledge, semi-supported plates have not been considered as ductile end diaphragms to date. Hence, there are not enough experimental studies. Therefore, to evaluate the accuracy of the numerical modelling, the verification study is separated into end diaphragm verification and semi-supported steel plate verification.

The experimental results for the short girder segment that were reported by Zahrai and Bruneau [9] were analysed to validate the modelling of the end diaphragm and the composite action between the concrete slab and steel girders. The end diaphragm modelling and the composite action among the steel girders ad concrete slab were validated by analysing the experimental results for the short girder segment that were reported by Zahrai and Bruneau [9]. The FE results slightly underestimated the experimental strength (by approximately 7%) up to the 25 mm drift amplitude (Figure 6 (a)). During the cycles over a 25-mm drift, strength loss was detected on the hysteretic diagrams. This loss cannot be captured through the FE simulation as the modelling of some secondary parameters is not considered. To evaluate the simulation of the semi-supported steel infill plate, the boundary conditions, and the modelling of initial imperfection, the experimental study conducted by Shekasteband et al. [24] was considered. The blue curve was drawn using the FE study and showed appropriate agreement between the experimental results and the numerical study (Figure 6 (b)).

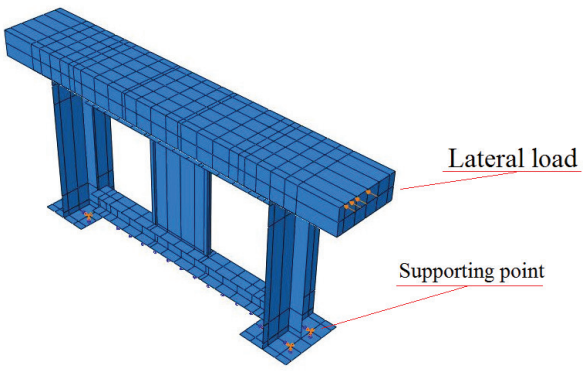

Figure 5. Support conditions and load case.

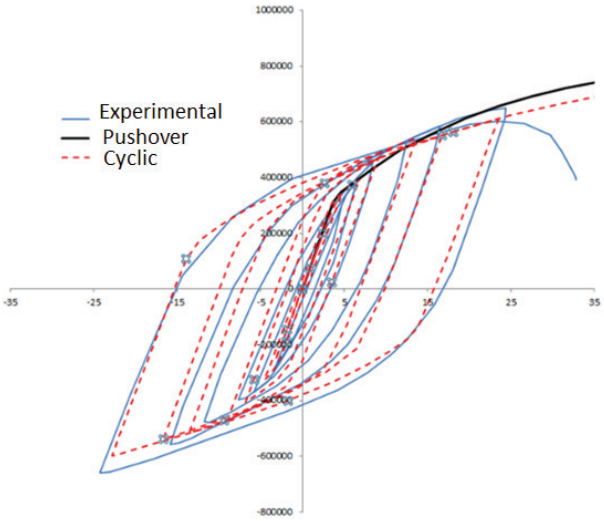

(a) Verification of end diaphragm capacity curve

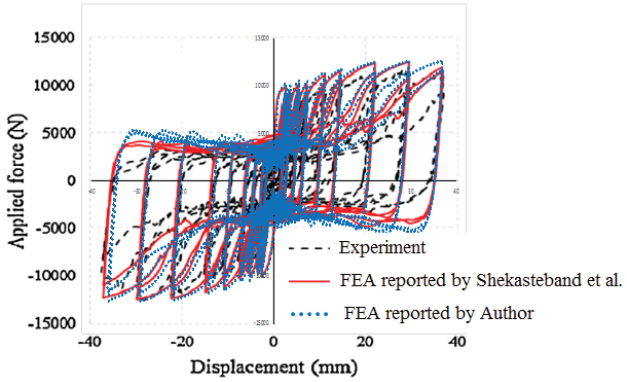

(b) Verification of SPSW capacity curve

Figure 6. Validation of numerical modelling.

RESULTS AND DISCUSSION

The capacity curves of all models extracted from push-over analysis (Figure 7) were replaced with an idealized curve based on the procedure illustrated in FEMA 356 [25] (Figure 8). This idealized curve is bilinear with initial slope, K_e, and post-yield slope,α. The effective stiffness, K_e, is taken as the scant stiffness calculated at a strength equal to 60% of the effective yield force, V_y. The post-yield slope, α, is determined via a straight line segment that passes through the actual capacity curve at the target displacement. FEMA 356 [25] and FEMA P695 [26] define the displacement corresponding to 20% decrease in the maximum strength of the diaphragm as ultimate displacement. Moreover, studies on SPSWs have shown that the structures suffered significant damages at 3% drift [27-29]. Hence, a minimum displacement corresponding to these two mentioned criteria was used as the target displacement.

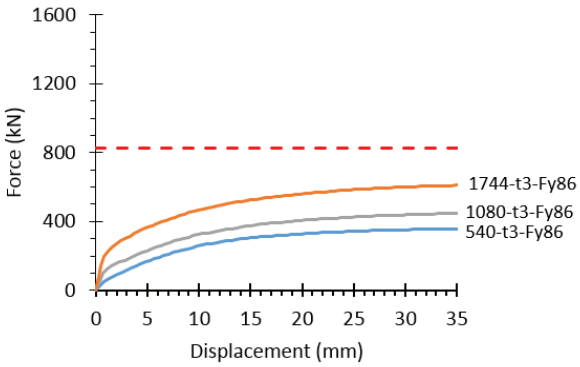

(a) 3 mm thickness Semi-supported Infill Plate with 86 MPa yielding stress

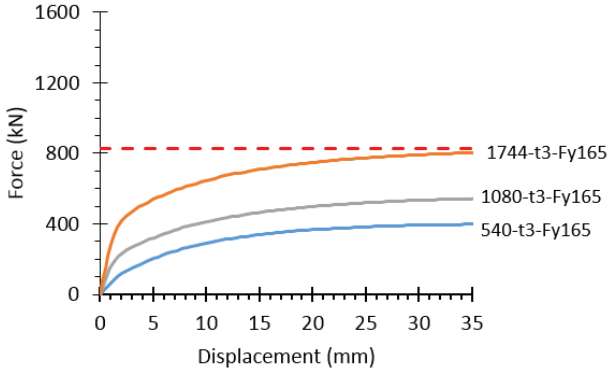

(b) 3 mm thickness Semi-supported Infill Plate with 165 MPa yielding stress

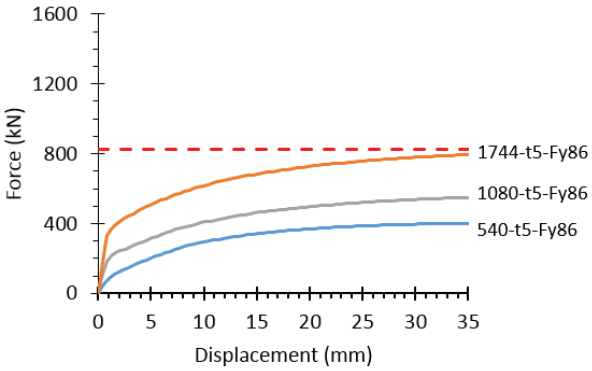

(c) 5 mm thickness Semi-supported Infill Plate with 86 MPa yielding stress

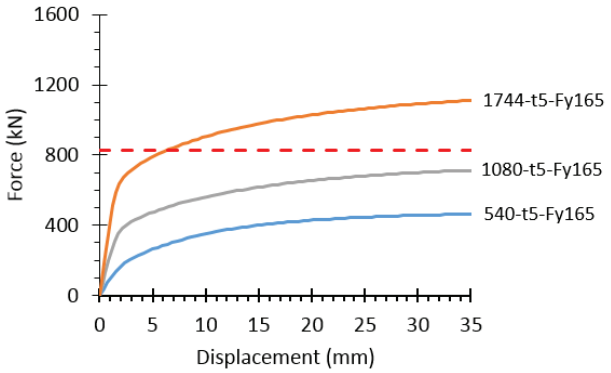

(d) 5 mm thickness Semi-supported Infill Plate with 165 MPa yielding stress

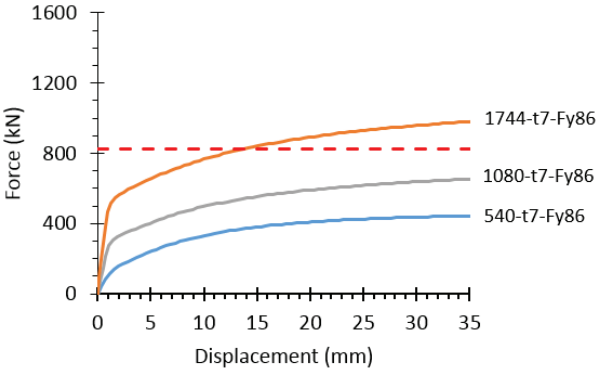

(e) 7 mm thickness Semi-supported Infill Plate with 86 MPa yielding stress

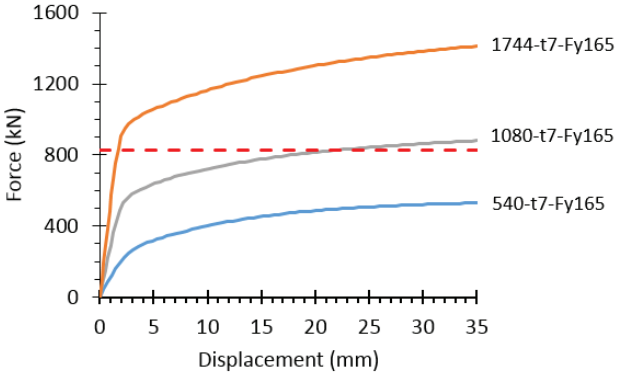

(f) 7 mm thickness Semi-supported Infill Plate with 165 MPa yielding stress

Figure 7. Capacity curve of all studied models.

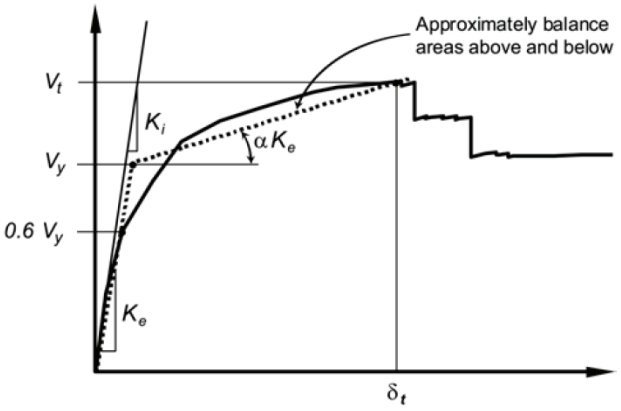

Figure 8. Idealized capacity curve.

The elastic lateral force was calculated based on AASHTO [30]. In this design specification, equivalent static earthquake loading is related to the seismic mass via an elastic seismic response coefficient, C_{sm}. C_{sm} is a function of the period of the bridge that is calculated by equation (1).

$$T = 2\,\pi\sqrt{\frac{m}{K}} \tag{1}$$

For slab on girder steel bridges, the bridge stiffness, K, is composed of the bridge end segment stiffness, K_{end}, the generalized stiffness of the superstructures, K^*, and the stiffness of the substructure, K_{sub}, (equation (2)) [8, 10].

$$K = \frac{1}{\frac{1}{K_{end}} + \frac{1}{K^*} + \frac{1}{K_{sub}}} \tag{2}$$

As this study concentrated on the single-span steel bridges supported on stiff substructures, the flexibility term of the substructure is neglected. K_{end} is obtained by adding the lateral stiffness provided by bearing stiffeners to the diaphragm stiffness. Based on the studied bridge dimensions and applied materials, m and K^* are calculated equal to $14583\ kg.sec^2/m$ and $272\ kN/mm$, respectively. The bridge periods due to the use of different semi-connected end plate diaphragms are provided in Table 3. As can be seen in Table 3, the period of all models lie within the constant acceleration region of the design response spectrum provided by AASHTO [30]. Therefore, elastic seismic response coefficient and consequently elastic force are constant for all models and are equal to 0.61 and 825 kN, respectively.

To dissipate seismic induced energy, ductile end diaphragms should be calibrated to yield before the elastic demand (825 kN) is reached. Hence the models, named 1744-t5-Fy165, 1744-t7-Fy86, 1080-t7-Fy165, and 1744-t7- Fy165 with effective yield force (as an illustrated in Figure 9) are equal to 1112, 982, 881 and 1413 kN, respectively, cannot be considered as a ductile end diaphragm (because $V_{y,eff}$ is greater than V_e). The von Mises stresses distribution (in N/mm^2) of 1744-t7-Fy165 (as an

Table 3. Stiffness and period of all models

Name of Models	K_e (kN/mm)	K_{end} (kN/mm)	K (kN/mm)	T (Sec)
540-t3-Fy86	33.19	46.47	39.69	0.38
1080-t3-Fy86	50.88	64.16	51.91	0.33
1744-t3-Fy86	135.21	148.49	96.05	0.24
540-t3-Fy165	41.73	55.01	45.76	0.35
1080-t3-Fy165	111.82	125.10	85.69	0.26
1744-t3-Fy165	242.34	255.62	131.78	0.21
540-t5-Fy86	41.26	54.54	45.43	0.35
1080-t5-Fy86	142.70	155.98	99.13	0.24
1744-t5-Fy86	371.37	384.65	159.33	0.19
540-t5-Fy165	66.96	80.24	61.96	0.30
1080-t5-Fy165	216.16	229.44	124.46	0.21
1744-t5-Fy165	406.64	419.92	165.07	0.18
540-t7-Fy86	55.80	69.08	55.09	0.32
1080-t7-Fy86	258.54	271.82	135.95	0.20
1744-t7-Fy86	506.40	519.68	178.55	0.18
540-t7-Fy165	94.26	107.54	77.07	0.27
1080-t7-Fy165	278.94	292.22	140.87	0.20
1744-t7-Fy165	512.91	526.19	179.31	0.18

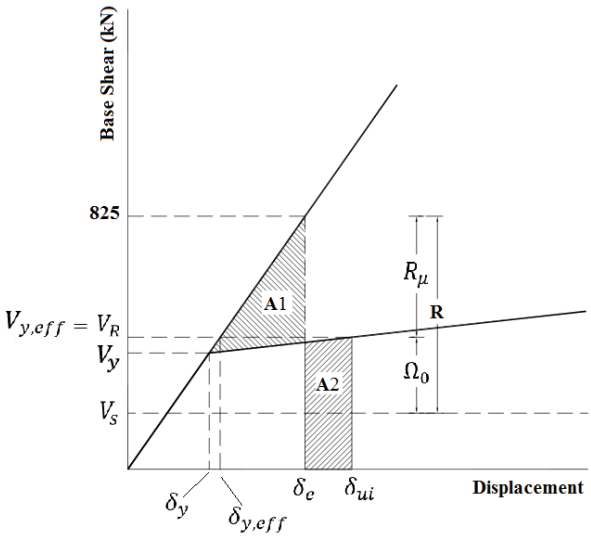

Figure 9. Response modification parameters on idealized curve.

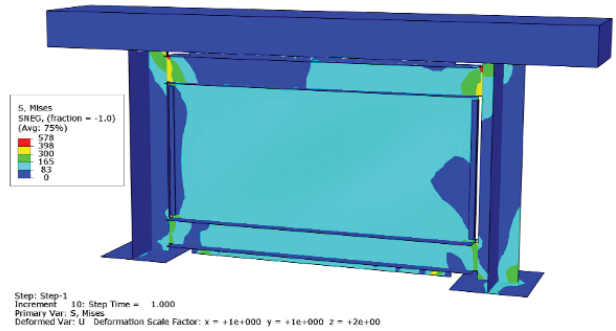

(a) 1744-t7-Fy165 as a nonductile end diaphragm

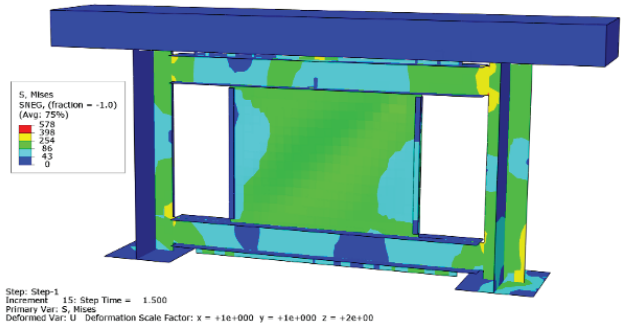

(b) 1080-t5-Fy86 as a ductile end diaphragm

Figure 10. Mises stresses distribution at δ_e corresponded to the elastic strength demand, 825 kN.

inappropriate diaphragm) and 1080-t5-Fy86 (as an appropriate diaphragm) at the displacement corresponded to the elastic demand, δ_e, are shown in Figure 10 (δ_e, is determined based on the linear elastic equation with a slope of K_e (Figure 9)). In Figure 10, the yielding zone is shown in green and red color for the semi connected thin plate and the surrounding frame, respectively. According to Figure 10(a), the semi-connected plate of the 1744-t7-Fy165 model doesn't yield at δ_e which shows the $7mm$ plate (with $F_y = 165\ Mpa$ and the length of 1744 mm) cannot be used as a dissipation energy device in a bridge demonstrated in section 2.1. However, in the 1080- t5-Fy86 model, a semi-connected thin plate significantly yields which shows a 5 mm plate (with $F_y = 86\ Mpa$ and the length of 1080 mm) can be used as a ductile end diaphragm in a bridge described in section 2.1 (Figure 10(b)).

Main girders adjacent to the semi-connected end plate diaphragms (SCEP) are considered a gravity load resisting system and should behave elastically. The stiffness degradation indicates the formation of a new plastic region and/or new structural damage. Therefore, tangent stiffness degradation of the SCEP diaphragms to less than the bare surrounding frame stiffness ($K_{bare} = 16.85\ kN/mm$) can be considered as a main girder damage criterion. Tangent stiffness at the elastic strength demand, $K_{e,t}$, of the remained models, were calculated and provided in Table 4. According to the mentioned main girder damage criterion, 540-t3-Fy86, 1080-t3-Fy86, 540-t3-Fy165, 540-t5-Fy86, 540-t5-Fy165, 540-t7-Fy86 and 540-t7-Fy165 with $K_{e,t}$ equal to 2.31, 6.68, 4, 4.04, 9.69, 7.22 and 13.89 kN/mm, respectively, cannot prevent the inelastic behavior of the main girders at the elastic strength demand. The

Table 4. Tangent stiffness at the elastic strength demand, $K_{e,t}$, of the ductile SCEP

Name of Models	δ_e (mm)	$K_{e,t}$ (kN/mm)	Name of Models	δ_e (mm)	$K_{e,t}$ (kN/mm)
540-t3-Fy86	24.86	2.31	1080-t5-Fy86	5.78	22.35
1080-t3-Fy86	16.22	6.68	1744-t5-Fy86	2.22	35.49
1744-t3-Fy86	6.1	22.61	540-t5-Fy165	12.32	9.69
540-t3-Fy165	19.77	4	1080-t5-Fy165	3.82	25.68
1080-t3-Fy165	7.38	18.37	540-t7-Fy86	14.78	7.22
1744-t3-Fy165	3.4	37.43	1080-t7-Fy86	3.19	24.48
540-t5-Fy86	19.99	4.04	540-t7-Fy165	8.75	13.89

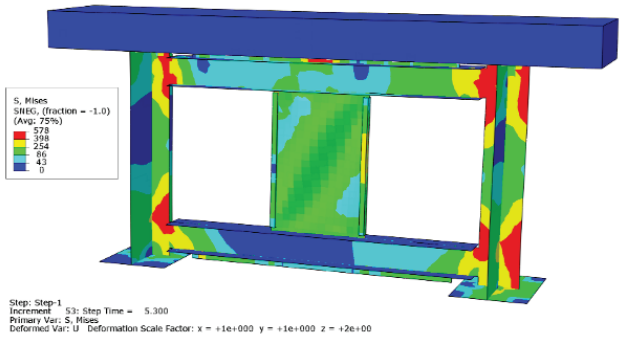

(a) 540-t3-Fy86 cannot be proposed a structural fuse.

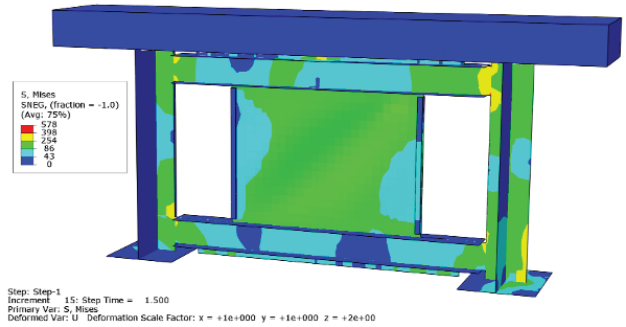

(b) 1080-t5-Fy86 can be proposed a structural fuse.

Figure 11. Mises stresses distribution at $_{\delta}$e.

von Mises stresses distribution of 540-t3-Fy86 (as an inappropriate diaphragm) and 1080-t5-Fy86 (as an appropriate diaphragm) at the displacement corresponded to the elastic demand, δ_e, are shown in Figure 11. According to Figure 11(a), the main girders yield at δ_e which shows the 5 mm plate (with $F_y = 86\ Mpa$ and the length of 540 mm) cannot be used as a structural fuse in the bridge superstructure demonstrated in section 2.1. However, in the 1080-t5-Fy86 model, the main girders don't yield at δ_y which shows a 5 mm plate (with $F_y = 86\ Mpa$ and the length of 1080 mm) can be used as a structural fuse in a bridge superstructure described in section 2.1 (Figure 11(b)).

Based on the ductile diaphragm definition and also the structural fuse concept, 1744-t3-Fy86, 1080-t3-Fy165, 1744-t3-Fy165, 1080-t5-Fy86, 1744-t5-Fy86, 1080-t5-Fy165 and 1080-t7-Fy86 are determined as the appropriate SCEP diaphragms. The optimum SCEP diaphragm is distinguished according to the response modification factor, R, which is extracted from the idealized capacity curve. In this order, the ultimate displacement of the idealized curve, δ_{ui}, is calculated through the assumption that the elastic response of the SCEP is restricted to the strength equal to 825 kN (Figure 9). Therefore, the area enclosed by the idealized capacity curve is calibrated to equal the area enclosed by the elastic response (in Figure 9 $A_1 = A_2$). The amount of δ_{ui} and V_R are calculated for the appropriate SCEP diaphragms and presented in Table 5.

$\delta_{y,eff}$ is calculated via equation (3) and then the ductility ratio, μ, is defined by equation (4).

$$\delta_{y,eff} = \frac{V_R}{K_e} \tag{3}$$

$$\mu = \frac{\delta_{ui}}{\delta_{y,eff}} \tag{4}$$

The ductility reduction factor, R_μ, can be expressed as a function of the ductility ratio [31]:

$$R_\mu = \sqrt{2\,\mu - 1} \tag{5}$$

In this study, the force reduction factor is calculated by equation (6):

$$R = R_\mu \Omega_0 \tag{6}$$

In equation (6), the overstrength factor is:

$$\Omega_0 = \frac{V_R}{V_s} \tag{7}$$

In equation (7), V_s is the strength at the first significant yield. The significant yield coincides with the significant stiffness reduction. Hence stiffness reduction diagram is used to determine the first significant yield. In Figure 12(a), the stiffness reduction bar chart is shown for 1080-t5-Fy86. According to this bar chart, the maximum stiffness reduction and consequently the first significant yield accrued at the displacement is equal to 0.86 mm corresponding to the 183.3 kN strength (Figure 12(b)). The von Mises stresses distribution of 1080-t5-Fy86 at the displacement corresponded to the first significant yield, δ_s, is shown in Figure 12(c). As shown in this figure, the first significant yield is concentrated in the SCEP which shows the appropriate performance of the proposed end diaphragm as a structural fuse in the bridge superstructure. Moreover, Figure 12(c) shows the diagonal tension field extension. Hence, although the seismic energy dissipates through the thin plate yielding, the residual stiffness and the increase in the strength of the SCEP diaphragm are considerable due to the diagonal tension field extension (such as the benefits reported for the steel plate shear wall). For all appropriate models, the response modification factors and all required parameters are calculated and presented in Table 5. As seen in Table 5, by increasing the thickness, the length, and/or the yielding stress of the appropriate semi-connected infill plate, the ductility and the response modification factor of the end diaphragms decrease. For example, the end diaphragms have a semi-connected plate with 1080 mm length and 86 MPa yielding stress, increasing the plate thickness from 5 (in model 1080-t5-Fy86) to 7 mm (in model 1080- t7-Fy86) decreases the ductility and the response modification factor from 2.63 to 2.1 and from 4.55 to 3.03, respectively. And

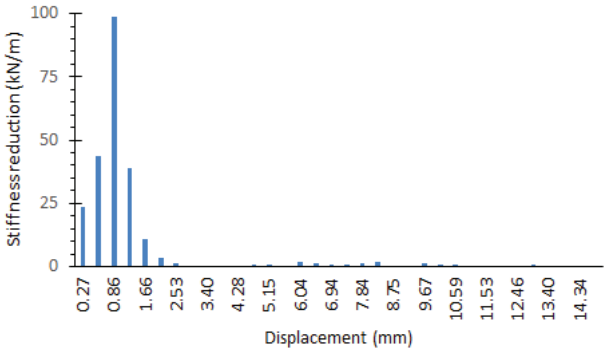

(a) Stiffness reduction diagram

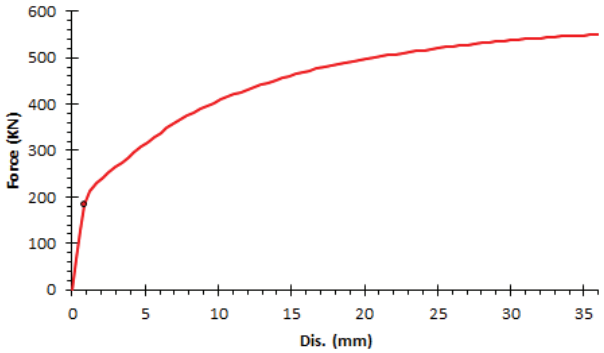

(b) Capacity curve

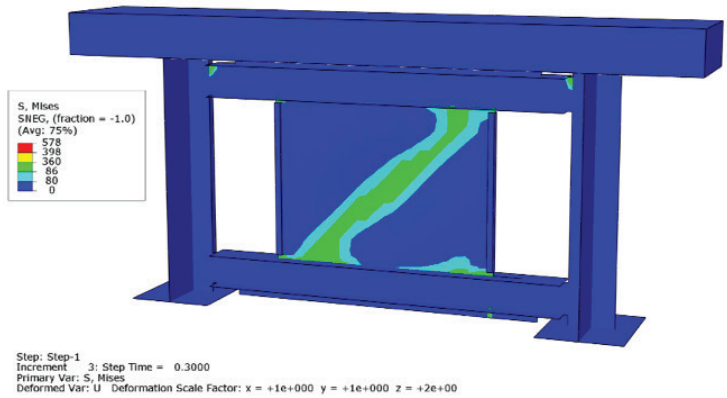

(c) Mises stresses distribution at at δ_s

Figure 12. Specify the first significant yield of the 1080-t5-Fy86.

Table 5. ductility and response modification factor parameters of appropriate SCEPs

Name of Models	δ_s (mm)	δ_y (mm)	$\delta_{y,eff}$ (mm)	δ_{ui} (mm)	V_s (kN)	V_y (kN)	V_R (kN)	μ	R_μ	Ω_0	R
1744-t3-Fy86	0.80	3.33	3.47	7.17	199	450	469	2.07	1.77	2.36	4.17
1080-t3-Fy165	1.31	3.55	3.78	9.26	188	397	423	2.45	1.97	2.25	4.44
1744-t3-Fy165	1.31	2.51	2.54	3.56	340	609	616	1.40	1.34	1.81	2.43
1080-t5-Fy86	0.86	2.66	2.83	7.46	183	379	404	2.63	2.07	2.20	4.55
1744-t5-Fy86	0.87	1.51	1.53	2.38	333	560	567	1.56	1.46	1.70	2.48
1080-t5-Fy165	1.42	2.44	2.48	4.19	311	527	537	1.69	1.54	1.73	2.66
1080-t7-Fy86	1.06	1.75	1.79	3.76	274	451	463	2.10	1.79	1.69	3.03

also increasing the length from 1080 (in model 1080-t5-Fy86) to 1744 mm (in model 1744-t5-Fy86) decreases the ductility and the response modification factor from 2.63 to 1.56 and from 4.55 to 2.48, respectively. Moreover, increasing the yielding stress from 86 (in model 1080-t5-Fy86) to 165 MPa (in model 1080-t5-Fy165) decreases the ductility and the response modification factor from 2.63 to 1.69 and from 4.55 to 2.66, respectively. Consequently, based on Table 5 the semi-connected end plate diaphragm with 86 MPa yielding stress, 5 mm thickness, and 1080 mm length infill plate (model 1080-t5-Fy86) is verified as an optimum diaphragm.

The hysteresis behavior of the appropriate SCEP diaphragms is studied through the cyclic analysis (such as the hysteresis curve of the 1080-t5-Fy86 shown in Figure 13). This analysis is conducted to investigate the energy dissipation capacity of a SCEP diaphragm up to ultimate displacement, δ_{ui}.

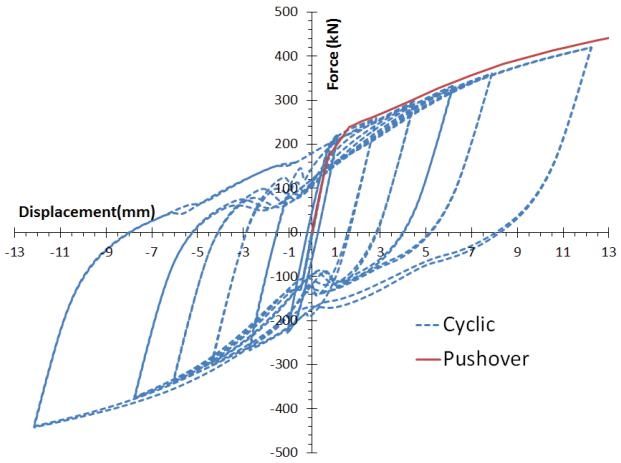

Figure 13. The hysteresis behavior of the 1080-t5-Fy86.

The amount of dissipated energy at each cycle is equivalent to the area enclosed by a load-displacement curve of the corresponding excursion. The energy dissipation capacity of a device is generally stated via the cumulative hysteretic energy dissipation (E_H) parameter, which is equivalent to the summation of the closed cycle's area (from the initial excursion up to the recent cycle). To compare the energy dissipation capacity of proper LYS infill plates, the normalized cumulative hysteretic energy dissipation parameter (E_{HN}), which is calculated by equation (8), is applied [32].

$$E_{HN} = \frac{E_H}{V_y \times \delta_y} \tag{8}$$

In Figure 14, the variation of the E_{HN} is drawn against the cumulative number of cycles. As can be seen in Figure 14, 1080-t5-Fy86 has the largest E_{HN} value and also the cumulative number of cycles, with amounts of 41.6 and 22,

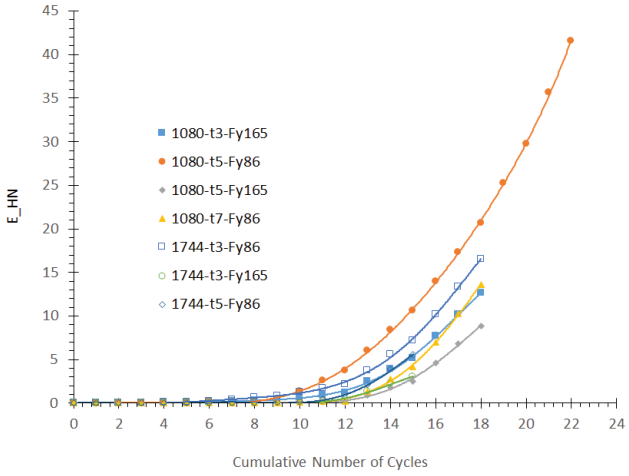

Figure 14. The variation of the E_{HN} versus the cumulative number of cycles.

Table 6. Equivalent viscous damping ratio of appropriate SCEPs

Name of Models	δ_{ui} (mm)	V_{ui} (kN)	E $(kN.mm)$	β_{eq} (%)
1744-t3-Fy86	7.2	407	4050	22.1
1080-t3-Fy165	9.3	384	4001	17.9
1744-t3-Fy165	3.6	479	1574	14.7
1080-t5-Fy86	7.5	354	3483	21.0
1744-t5-Fy86	2.4	414	1514	24.4
1080-t5-Fy165	4.2	438	2024	17.6
1080-t7-Fy86	3.8	367	2512	29.0

respectively. This also indicates that the semi-connected end plate diaphragm with 86 MPa yielding stress, 5 mm thickness, and 1080 mm length infill plate (model 1080-t5-Fy86) is the optimum diaphragm for the studied bridge.

Equivalent viscous damping ratio, β_{eq}, is calculated via equation (9) and based on the cyclic hysteresis date corresponded to the ultimate displacement:

$$\beta_{eq} = \frac{E}{2\,\pi V_{ui}\delta_{ui}} \tag{9}$$

The closed cycle's area, E, and equivalent viscous damping ratio, β_{eq}, of all appropriate diaphragms are provided in Table 6. The equivalent viscous damping ratio of model 1080-t5-Fy86 is calculated as 21%. This value is appropriate for ductile performance.

CONCLUSION

Eighteen semi-connected end diaphragm panels with different infill plate thicknesses, different lengths, and different types of steel materials were used to enhance the seismic performance of steel girder bridges.

The following summarizes were resulted through the parametric studies:

- To dissipate seismic induced energy, the infill plate should be yielded before the elastic demand (825 kN) is reached. Excessive increases in the infill plate length and thickness lead to the elastic behaviour of SCEP diaphragms. According to this study, the models named 1744-t5-Fy165, 1744-t7-Fy86, 1080-t7-Fy165, and 1744-t7-Fy165 are considered nonductile end diaphragms.
- Main girders are considered a gravity load resisting system and should stay behave elastically. Too much reduction of the infill plate length and thickness concentrate damage to the bearing stiffeners of the main girders. Based on this study, the models named 540-t3-Fy86, 1080-t3-Fy86, 540-t3-Fy165, 540-t5-Fy86, 540-t5-Fy165, 540-t7-Fy86, and 540-t7-Fy165 cannot be considered as a structural fuse.

- The optimum SCEP diaphragm is distinguished according to the response modification factor, R. According to this study, the model 1080-t5-Fy86 with a 4.55 response modification factor is verified as an optimum diaphragm.
- The variation of the normalized cumulative hysteretic energy dissipation is studied against the cumulative number of cycles through the cyclic analysis. The results show that 1080-t5-Fy86 has the largest E_{HN} value and also the cumulative number of cycles, with amounts of 41.6 and 22, respectively.

NOMENCLATURE

C_{sm}	Elastic seismic response coefficient.
E_H	Cumulative hysteretic energy dissipation, $kN.mm$.
E_{HN}	Normalized cumulative hysteretic energy dissipation parameter, $kN.mm$.
K	Bridge stiffness, kN/mm.
K^*	Generalized stiffness of the superstructures, kN/mm.
$Kbare$	Bare surrounding frame stiffness, kN/mm.
K_e	Effective stiffness, kN/mm.
K_{end}	Bridge end segment stiffness, kN/mm.
$K_{e,t}$	Tangent stiffness at the elastic strength demand, sec.
K_{sub}	Stiffness of the substructure, kN/mm.
R	Response modification factor.
R_μ	Ductility reduction factor.
T	Period of the bridge, Sec.
V_s	Strength at the first significant yield, kN.
V_y	Yield force, kN.
$V_{y,eff}$	Effective yield force, kN.

Greek symbols

α	Post-yield slope.
β_{eq}	Equivalent viscous damping ratio.
δ_e	Elastic demand, mm.
δ_s	Displacement corresponded to the first significant yield, mm.
δ_{ui}	Ultimate displacement of the idealized curve, mm.
δ_y	Yield displacement, mm.
$\delta_{y,eff}$	Effective yield displacement, mm.
μ	Ductility ratio.
Ω_0	Overstrength factor.

ACKNOWLEDGMENTS

This research was supported by the Islamic Azad University, Chalous Branch

AUTHORSHIP CONTRIBUTIONS

Authors equally contributed to this work.

DATA AVAILABILITY STATEMENT

The authors confirm that the data that supports the findings of this study are available within the article. Raw data that support the finding of this study are available from the corresponding author, upon reasonable request.

CONFLICT OF INTEREST

The author declared no potential conflicts of interest with respect to the research, authorship, and/or publication of this article.

ETHICS

There are no ethical issues with the publication of this manuscript.

REFERENCES

[1] Astaneh-Asl A, McMullin KM, Cho SW. Seismic performance of steel bridges during the 1994 Northridge earthquake. Restruct America Beyond 1994. ASCE.

[2] Bruneau M, Wilson JC, Tremblay R. Performance of steel bridges during the 1995 Hyogo-ken Nanbu (Kobe, Japan) earthquake. Can J Civil Eng 1996;23:678–713. [CrossRef]

[3] Itani AM, Bruneau M, Carden L, Buckle IG. Seismic behavior of steel girder bridge superstructures. J Bridge Eng 2004;9:243–249. [CrossRef]

[4] Zahrai SM, Bruneau M. Impact of diaphragms on seismic response of straight slab-on-girder steel bridges. J Struct Eng 1998;124:938–947. [CrossRef]

[5] Jamshidi M, Majid TA, Bunnori NM. Seismic behaviour of slab-on-girder steel bridges equipped with ductile steel infill plate end diaphragms. Int J Steel Struct 2015;15:459–472. [CrossRef]

[6] ASTANEH-ASL A. Notes on the cyclic behavior and design of steel bridges in Technical report. 1996. American Iron and Steel Institute: USA.

[7] Bahrami H, Itani AM, Buckle IG. Guidelines for the seismic design of ductile end cross frames in steel girder bridge superstructures. Center for Civil Engineering Earthquake Research (CCEER), 2010.

[8] Jamshidi M, Majid TA. Seismic retrofit of slab-on-girder steel bridges. Proceed Inst Civil Eng Struct Build 2017;170:521–531. [CrossRef]

[9] Zahrai SM, Bruneau M. Cyclic testing of ductile end diaphragms for slab-on-girder steel bridges. J Struct Eng 1999;125:987–996. [CrossRef]

[10] Zahrai SM, Bruneau M. Ductile end-diaphragms for seismic retrofit of slab-on-girder steel bridges. J Struct Eng 1999;125:71–80. [CrossRef]

[11] Carden LP, Itani AM, Buckle IG. Seismic performance of steel girder bridges with ductile cross frames using buckling-restrained braces. J Struct Eng 2006;132:338–345. [CrossRef]

[12] Carden LP, Itani AM, Buckle IG. Seismic performance of steel girder bridges with ductile cross frames using single angle X braces. J Struct Eng 2006;132:329–337. [CrossRef]
[13] Dolati A, Maleki S. Ductile behavior of existing internal end diaphragms in steel tub girder bridges. J Construct Steel Res 2019;153:356–371. [CrossRef]
[14] Jahanpour A, Moharrami H. Evaluation of behavior of the secondary columns in semi-supported steel shear walls. Thin-Walled Struct 2015;93:94–101. [CrossRef]
[15] Guo L, Rong Q, Qu B, Liu J. Testing of steel plate shear walls with composite columns and infill plates connected to beams only. Eng Struct 2017;136:165–179. [CrossRef]
[16] Shekastehband B, Azaraxsh A, Showkati H. Experimental seismic study on shear walls with fully-connected and beam-only-connected web plates. J Construct Steel Res 2018;141:204–215. [CrossRef]
[17] Ozcelik Y, Clayton PM. Seismic design and performance of SPSWs with beam-connected web plates. J Construct Steel Res 2018;142:55–67. [CrossRef]
[18] Dicleli M, Bruneau M. Seismic performance of single-span simply supported and continuous slab-on-girder steel highway bridges. J Struct Eng 1995;121:1497–1506. [CrossRef]
[19] American Association of State Highway Officials. Manual for Signing and Pavement Marking of the National System of Interstate and Defense Highways: Revisions Adopted November 26, 1960 by the American Association of State Highway Officials; Revisions Approved December 16, 1960. 1961: American Association of State Highway Officials.
[20] Carden L, Itani AM, Buckle IG. An Experimental Study into the Distribution of Earthquake Forces in Steel Plate Girder Bridges. in Proceedings of the Pacific Conference on Earthquake Engineering, Christchurch, New Zealand. Paper. 2003.
[21] Bahrami H, Buckle IG, Itani AM. Seismic response of steel bridges with decoupled ductile end-cross frames. in Georgia Institute of Technology-US-Italy Seismic Bridge Workshop. 2007.
[22] Sabelli R, Bruneau M. Design guide 20: steel plate shear walls, American Institute of Steel Construction. Chicago, IL, USA, 2007.
[23] Zahrai SM, Bruneau M. Seismic retrofit of slab-on-girder steel bridges using ductile end diaphragms. Report No. OCEERC, 1998; p. 98–20.
[24] Shekastehband B, Azaraxsh A, Showkati H. Experimental and numerical study on seismic behavior of LYS and HYS steel plate shear walls connected to frame beams only. Arch Civil Mech Eng 2017;17:154–168. [CrossRef]
[25] FEMA. Prestandard and commentary for the seismic rehabilitation of buildings, in Report FEMA-356, Washington, DC. 2000.
[26] FEMA. Quantification of building seismic performance factors. Report No. FEMA P695. 2009: Washington D.C.
[27] Vian D. Steel plate shear walls for seismic design and retrofit of building structures. New York: State University of New York at Buffalo; 2005.
[28] Behbahanifard MR, Grondin GY, Elwi AEA. Experimental and numerical investigation of steel plate shear walls. University of Alberta, Department of Civil and Environmental Engineering, 2003.
[29] Sabouri-Ghomi S, Gholhaki M. Tests of two three-story ductile steel plate shear walls. in Structures Congress 2008: Crossing Borders. 2008. [CrossRef]
[30] American Association of State Highway and Transportation Officials. AASHTO LRFD Bridge Design Specifications. 8th ed. Washington, D.C.: American Association of State Highway and Transportation Officials; 2017.
[31] Newmark NM, Hall WJ. Earthquake Spectra and Design. El Cerrito, Calif: Earthquake Engineering Research Institute; 1982,
[32] Berman JW, Celik OC, Bruneau M. Comparing hysteretic behavior of light-gauge steel plate shear walls and braced frames. Eng Struct 2005;27:475–485. [CrossRef]